Investigation of Thermal Cycle and Hardness Distribution in the Laser Cladding of AISI H13 tool steel produced by a High Power Direct Diode Laser

Parisa Farahmand
pfarahmand@smu.edu

Prabu Balu

Fanrong Kong

Radovan Kovacevic
kovacevi@smu.edu

Recommended Citation

IMECE2013-62193

Investigation of Thermal Cycle and Hardness Distribution in the Laser Cladding of AISI H13 tool steel produced by a High Power Direct Diode Laser

Parisa Farahmand	**Prabu Balu**	**Fanrong Kong**	**Radovan Kovacevic**
RCAM, SMU	RCAM, SMU	RCAM, SMU	RCAM, SMU
Dallas, Texas, USA	Dallas, Texas, USA	Dallas, Texas, USA	Dallas, Texas, USA

Abstract

Laser cladding (LC) of tool steel has significant application in rapid tooling, and surface coating for worn-out components in different industries. During the LC process, several phase transformations influence the microstructural and mechanical properties of the deposited layer. In order to successfully implement the LC process, it is essential to understand the relationship between the thermal cycle (heating and cooling), phase transformations, and the output quantities of the deposited layer. In this study a direct diode laser with a power of up to 8 kW was used to deposit AISI H13 tool steel on mild steel grade A36 substrate to enhance its surface properties. Primarily, an experimentally verified three-dimensional (3-D) heat transfer analysis was developed based on the finite element method to compute temperature history during the cladding and cooling process. Next, the computed thermal cycles were coupled with a semi-empirical thermo-kinetic model to estimate the hardness of deposited layers based on different cooling cycles in a time-temperature-transformation (TTT) diagram. Further, the microstructural details obtained from the cross-sections of the clad were correlated with the estimated thermal cycles and hardness. A good correlation between the modeled and experimental results revealed that the developed model can be used to estimate the microstructural characteristics and mechanical properties of the H13 layer produced by the LC process.

Key Words Laser cladding, finite element method, phase transformation, thermo-kinetic model, hardness prediction.

Introduction

Laser cladding (LC) is a well recognized technology for improving the performance of components against aggressive wear, corrosion, and erosive conditions [1]. In comparison with other conventional techniques like hardfacing by arc welding, and high velocity oxyfuel thermal spraying, the LC produces a metallurgical bond with low dilution, low porosity and good surface uniformity [2]. In this process, a coating material in the form of wire or powder is added into the molten pool created by a laser beam on the substrate in order to form a coating layer. In general, powder as filler material is widely accepted in LC in versus wire and strip because of the availability of most of the metals and alloys in powder form [3]. In a typical industrial application, the coating produced by LC needs to meet the following attributes: (1) superior mechanical properties, (2) good metallurgical bond at the substrate/coating interface, and (3) minimal dilution [4, 5]. The coating quality and its performance depend on microstructural evolution and the mechanical properties of the deposited material. The thermal cycle (heating and cooling) during the LC process affects the phase transformation kinetics and subsequently, influences the mechanical properties [6]. Thus, it is necessary to control the thermal cycle in order to achieve the desired clad quality. However, controlling the thermal cycle and heat evolution in cladding is complex due to the interaction among the laser beam, powder particles, and molten pool [7]. For example, Hofman et al. [8] reported that in a typical LC, injected powder caused a fluctuation of

the absorbed energy by the substrate. In other words, they reported that a large portion (87%) of laser energy is attenuated by the powder for heating up [8]. In addition, the presence of a steep cooling rate (on the order of 10^4 $^{\circ}$C/s) caused by high input energy and a large amount of the dissipated heat in the substrate makes control of the heat evolution more complex [4, 5].

In order to understand the different complex phenomena involved in LC process, mathematical modeling is becoming an effective method. Several analytical and numerical methods have been developed to solve energy, mass, and momentum equations as well as prediction of the effect of process parameters (i.e., laser power, scanning speed, and powder flow rate). Mazumder and Steen [9] developed an analytical heat transfer model that incorporated the effect of surface tension on the enhancement of molten pool convection in the laser surface treatment. Kar and Mazumder [10] developed a one-dimensional (1-D) analytical model to determine the coating composition according to the thermal cycle in LC. In 1994, Picasso et al. [7] developed a comprehensive 3-D analytical model to calculate the molten pool size and powder catchment efficiency. They studied the effects of the powder feed rate and scanning speed in multi-track cladding. Hofman et al. [8] developed a mathematical model to control the molten pool size and dilution. They found that a molten pool with a size less than 90% of the laser beam diameter resulted in minimal dilution. Kim and Peng [11] utilized a two-dimensional (2-D) finite element model to control the dilution in cladding using a Nd:YAG laser. They showed that thermal conductivity of the base metal in LC is an important physical property that determines the molten pool size and the dilution. Amara et al. [12] used a finite difference method combined with a dynamic mesh to identify the clad profiles as a function of laser power, mass flow rate of powder, and material properties. Kong and Kovacevic [13] developed a 2-D multi-phase transient model for multilayered cladding. They investigated the effects of laser power, scanning speed, and powder flow rate on clad geometry and remelted depth of each deposited layer. Wen and Shin [14] developed a comprehensive 3-D transient model based on a level set approach for multi-track direct laser deposition. They showed the cooling rate during the LC process for steel was around 2.5×10^4 K/s. Toyserkani et al. [15] proposed a 3-D transient finite element model to represent the clad geometry as a function of time and process parameters in a pulsed laser-based cladding. The model was used to study the influence of laser power, scanning speed, laser pulse shaping, and

power is absorbed by the substrate, while a small portion (13%) of laser temperature-dependent material properties. Fallah et al. [16] used a 3-D transient finite element method to estimate the molten pool dimension, clad profile, and solid/liquid interface profile of Ti45Nb cladding using a fiber laser. Their model evaluated the clad thickness, temperature gradient, and interface velocity along the solid/liquid interface. A 3-D heat transfer model for cladding copper powder on SS316 was developed by Kumar et al. [17]. Their study showed the importance of thermal conductivity enhancement in controlling the molten pool size and the final clad shape. Bruckner et al. [18] proposed a very detailed 3-D finite element model that determined the bead shape, the influence of process parameters, and the material properties in LC. Balu et al. [19] studied the temperature evolution and effects of process parameters and mass fraction of reinforcement in the LC of single and multilayer deposits of Ni-WC composite material by using an experimentally verified 3-D heat transfer model.

The final mechanical properties of the deposit are also closely related to its final microstructure, which has been experimentally and numerically verified to be in a direct relationship with thermal history in cladding. A number of studies showed that the distribution of hardness in coating can be estimated by coupling the modeled thermal history to thermo-kinetic equations. Li et al. [20] presented a thermo-kinetic model for the surface heat treatment of steel. Based on this model, the microstructure variation and hardness distribution were predicted. Costa et al. [4] developed a thermo-kinetic model for multilayer laser powder deposition. They investigated the final microstructure and hardness distribution in a multilayered wall deposition. In a similar way, Wang et al. [21] studied the effects of laser power and scanning speed on the cladding of stainless steel 410. Foroozmehr et al. [5] studied the effect of the scanning path on the temperature history and hardness of the AISI 4140 clad. They showed that the direction of the scanning path would affect the microstructure and hardness distribution. He et al. [6] developed a 3-D mathematical model to predict the temperature and composition distribution during the multi-track cladding of H13 tool steel. It was shown that phase transformation in the second layer of deposited material was affected by the previously deposited layer and preheating during the LC. Manvatkar et al. [22] used a 3-D heat transfer analysis to compute the thermal cycle in multilayered deposition. They used the thermal cycle to estimate the cell sizes as the structural parameter and hardness distribution of a solid structure.

2

To date, there are several studies carried out to estimate the thermo-metallurgical phenomena in LC. However, the thermal behavior and phase transformation kinetics of different materials depend on the type of the laser used and the heat distribution. In this study, chromium-molybdenum hot-work tool steel (H13) was deposited on mild steel grade A36 using a high power direct diode laser (HPDDL) with a maximum power of 8 kW. The H13 steel is a typical material used as protective coating on large-sized parts (e.g., die and mold). H13 is used especially for its high temperature and corrosive atmosphere due to its high anticorrosion potential and combination of resistance to high temperature softening and toughness. HPDDL, in comparison to the other types of lasers (e.g., CO_2 and Nd:YAG) offers several advantages including superior coating quality, very low dilution, better morphological characteristics, fewer cracks, and less porosity generation [23,24]. In addition, the large and rectangular shape of the HPDDL beam has a uniform input power density (top hat). Meanwhile, fewer scanning tracks to cover a specified area are required [25]. The main objective of this study is to develop an experimentally verified 3-D heat transfer model incorporating temperature and directionality dependent material properties using the commercial software ANSYS 11.0 to compute temperature history and cooling rates during cladding. First, the computed result (thermal cycle) is validated with the corresponding measured results in a single layer laser deposition of H13 steel. Next, the modeled thermal cycle is coupled with an empirical thermo-kinetic relationship based on the Koistinen-Marburger equation to estimate the hardness distribution in the clad. Further, the microstructural details obtained from the cross sections of the clad are correlated with the estimated thermal cycles and hardness. The metallurgical characterization by optical microscopy (OM) and hardness measurement is used to quantify the effect of process parameters on hardness, microstructure, and HAZ depth.

Experimental setup and procedures

The experiments were performed using an 8 kW direct diode laser of 975 nm wavelength and a 6-axis KUKA robot. The experimental setup is shown in Fig. 1, which includes a powder feeder, control unit for controlling the output power, chiller for cooling the laser head and cladding nozzles during the process (see Fig1.a). The powder was transported through two symmetric co-axial nozzles with seven channels (1 mm $\times$ 1 mm) that are in 35° tilted angle in respect to the vertical axis (see Fig 1.b). Argon was

used as a carrier gas as well as a shielding gas (protecting the melt pool from oxidation). The laser spot had a rectangular shape with 12 mm (slow axis) $\times$ 3 mm (fast axis) dimension and uniform power distribution (top hat).
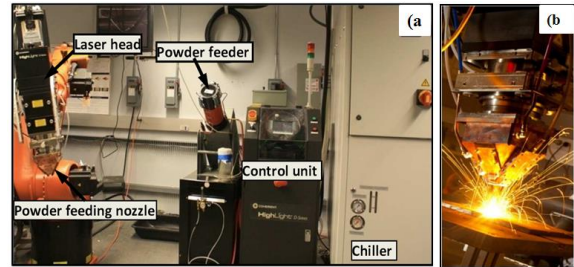

Fig. 1 (a) Experimental setup for laser cladding process, (b) Laser head and powder nozzle system.

Mild steel ASTM A36 was used as the substrate, the coupons were cut by an abrasive water-jet cutting machine with the dimensions 70 mm $\times$ 30 mm $\times$ 5 mm (length by width by thickness). The surface was cleaned by sandpaper and acetone to remove the rust and to make a smooth surface prior to cladding. Chromium-molybdenum hot work tool steel, AISI H13 powder, at an average particle diameter of 90 μm was used as a coating material (Fig. 2). The H13 tools steel is widely used in the die and mold making industry because of its high strength and resistance to wear, thermal shock, and corrosion. Its moderate cost makes it a first choice for protective coating in large and expensive parts exposed to corrosive and high temperature working conditions [26, 27]. The chemical composition of the substrate and powder are summarized in Table 1.
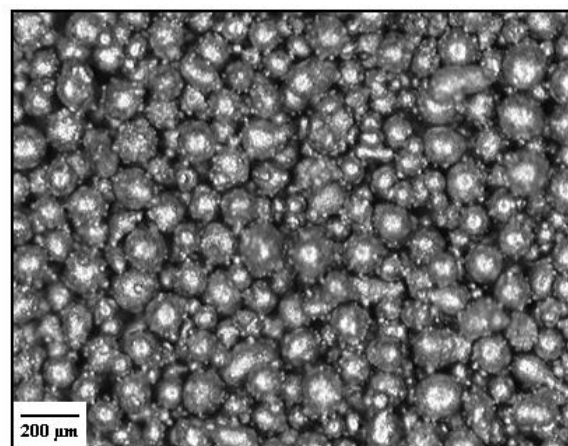

Fig. 2 Microscope image of the powder H13.

3

Table 1- Chemical composition of ASTM A36 and AISI H13 [28].

Steel	Chemical composition, % by weight										
	C	**Si**	**Mn**	**S**	**P**	**Ni**	**Cr**	**Cu**	**Mo**	**V**	**Fe**
ASTM A36	0.23	0.02	0.49	0.01	0.01	0.01	_	0.03	_	_	Bal.
AISI H13	max.0.4	1.0	0.3	_	_	_	max.5.3	_	max.1.4	1.0	Bal.

Table 2- Process parameters for deposition of H13 on mild steel A36

Ex. no	Laser power(W)	Scanning Speed(mm/s)	Powder feed rate (g/s)
1	4100	3	0.75
2	3500	3	0.75
3	4100	5	0.75
4	3500	5	0.75

In order to measure the temperature during the laser cladding process, a chromel-alumel (K type) thermocouple, with the capability to measure the maximum temperature 1100 ^{o}C, was used. The operation parameters are listed in Table 2.The cross section of cladded coupons after cutting and mounting, were prepared for metallographic and hardness testing following the standard polishing procedure. After completing the polishing procedure, the coupons were etched with 3% Nital solution to reveal the clad microstructure and morphology of HAZ. Dimensions of the cladded area (i.e., clad height (h_1) and width (w_1)) and the HAZ boundary (i.e., depth (h_2) and width (w_2)) were measured by the ultra high-resolution optical microscope; a cross-sectional view is shown in Fig. 3. The optical microscope with a magnification of 1000 X was used for microstructure characterization for clad and substrate. The hardness of the clad was obtained by taking an average of the measurements with 0.3 mm increments along the clad height and 1.5 mm increments along the width from the center line of each coated layer using a digital micro-hardness tester. A load of 500 gf with a dwell time of 15 s was used in the hardness test.

Thermal finite element model (FEM)

In order to calculate the temperature history and cooling cycles during the deposition process, a 3-D heat transfer model based on the finite element method was developed using commercial software ANSYS(11.0). By using the element kill-and-birth technique available in the ANSYS Parametric Design Language (APDL), the additive nature of powder deposition process was modeled
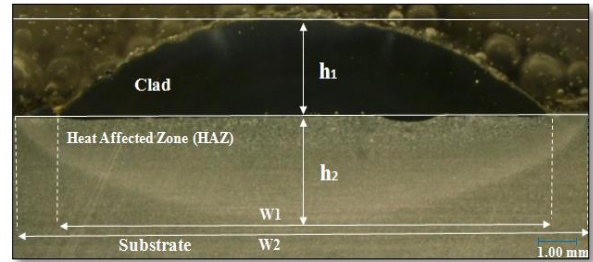

Fig. 3 Cross-section micrograph of the cladded coupon (4100W, 3 mm/s, 0.75g/s).

Thermal finite element model (FEM)

In order to calculate the temperature history and cooling cycles during the deposition process, a 3-D heat transfer model based on the finite element method was developed using commercial software ANSYS(11.0). By using the element kill-and-birth technique available in the ANSYS Parametric Design Language (APDL), the additive nature of powder deposition process was modeled.

Governing equations

The transient energy balance equation in the Cartesian coordinates can be given as follow:

$$\frac{\partial(\rho(T).C_P(T).T)}{\partial t} = \frac{\partial}{\partial x}\left(K_x(T).\frac{\partial T}{\partial x}\right) + \frac{\partial}{\partial y}\left(K_y(T).\frac{\partial T}{\partial y}\right) + \frac{\partial}{\partial z}\left(K_z(T).\frac{\partial T}{\partial z}\right) + \Gamma \qquad (1)$$

Where ρ (T) (Kg/m^3) is the temperature dependent material density, C_p (J/kg^{o}C) is the temperature dependent material specific heat, and Γ is the latent heat that is associated in the temperature dependent specific heat, and $K_i(T)$ (W/m^{o}C) is the temperature

4

Table 3- Temperature-dependent thermal properties of ASTM A36 and H13 tool steel [27, 29].

ASTM A36

Temperature (^{o}C)	**25**	**100**	**200**	**400**	**600**	**800**	**1000**	**1200**	**1400**	**1600**	**1800**	**2000**
Specific heat (J/kg ^{o}C)	480	500	520	650	750	1000	1200	1400	1600	1700	1700	1700
Conductivity (W/(m ^{o}C))	60	50	45	38	30	25	26	28	37	37	37	37
Density (kg/m^3)	7650	7650	7600	7580	7550	7200	7150	7100	7000	7000	6900	6900

AISI H13

Temperature (^{o}C)	**25**	**100**	**200**	**400**	**600**	**800**	**1000**	**1200**	**1400**	**1600**	**1800**	**2000**
Specific heat (J/kg ^{o}C)	447	453	467	502	537	572	607	642	677	708	721	721
Conductivity (W/(m ^{o}C))	29.5	30.3	33.7	37	40.5	43.9	47.3	50.7	21.98	24.06	25	25
Density (kg/m^3)	7650	7650	7600	7580	7550	7200	7150	7100	7000	7000	6900	6900

and directionally-dependent thermal conductivity. When the solution temperature is higher than the melting temperature (1480°C), the thermal conduction in each of the three directions (x, y, z) is enhanced by a multiplying factor of ξ_k that incorporates the effect of Marangoni-Rayleigh-Benard convection in heat transfer of the molten pool [17]. The temperature-dependent material properties of mild steel A36 and H13 are summarized in Table 3.

Initial and boundary conditions

The initial temperature of a substrate at room temperature (25°C) can be given as:

$$T(x, y, z, t = 0) = T_0 \tag{2}$$

It was assumed that the temperature distribution in the substrate and deposit attains room temperature after the cooling process, and it is represented as:

$$T(x, y, z, t = \infty) = T_0 \tag{3}$$

During the LC process, the molten pool cools down by conducting heat through the solid substrate and by losing some of its energy to the ambient air through the thermal radiation and convection. Therefore, the heat lost by convection and radiation, assumed as boundary conditions in the governing equation, are generally expressed by Eq. (4):

$$k(\nabla T . \vec{n})|_\Omega = \begin{cases} h(T - T_0) + \varepsilon\sigma((T + 273)^4 - (T_0 + 273)^4) - Q_{laser} & \Omega \in \Gamma \\ h(T - T_0) + \varepsilon\sigma((T + 273)^4 - (T_0 + 273)^4) & \Omega \notin \Gamma \end{cases} \tag{4}$$

where $\vec{n}$ is the normal vector of surface, h is the convection coefficient (W/m^{2o}C), T is the surface temperature (^{o}C), T_o is the room temperature (25°C), σ is the Stefan Boltzman constant (5.67×10^{-8} W/m^{2}K^4), and ε is the substrate emissivity (ε = 0.3) [30]. Γ is the substrate surface that is exposed to laser irradiation and the shielding gas. The effects of radiation and convection are combined into a "lumped" heat transfer coefficient. At the top surface

where shielding gas contributes to the cooling, the heat transfer coefficient was set at 180 W/m^{2o}C. Whereas at the sides and the bottom, the values of 100 W/m^{2o}C and 60 W/m^{2o}C were considered, respectively. These values were chosen according to the best correlation between calculated and measured temperature. The power density distribution of HPDDL is of a rectangular shape with a uniform "top-hat" profile. In the analysis, the heat source is expressed as a uniform-rectangular heat source [31]:

$$Q_{laser} = \begin{cases} \dfrac{P \times \mu}{W \times L} & \text{for } -\dfrac{l}{2} \le x - v.t \le \dfrac{l}{2} \text{ and } \dfrac{-w}{2} \le y \le \dfrac{w}{2} \\ 0 & \text{otherwise} \end{cases} \tag{5}$$

where P is laser power (W), μ is the substrate absorption coefficient, W is the laser spot width (12 mm) along the Y-axis, and L is the laser spot length (3 mm) along the X-axis of the substrate. The effective laser absorption coefficient (μ) for substrate is calculated according to Bramson`s equation:

$$\mu = 0.365(R/\lambda)^{1/2} - 0.067(R/\lambda) + 0.006(R/\lambda)^{3/2} \tag{6}$$

where R is temperature-dependent electrical resistivity, and λ is a wavelength of the laser beam (975 nm). The electrical resistivity of mild steel A36 is 16 $\mu\Omega$ at 27 ^{o}C and 110 $\mu\Omega$ at 800 ^{o}C, respectively [32]. By averaging the calculated values of the absorption coefficient for the different temperatures, the value of the effective absorption was found to be 0.3.

Bead shape

In the typical LC process, when powder particles are impinging onto the molten pool surface, the molten pool free surface resembles the shape of an ellipsoid [19]. The model used to determine the molten pool surface along the scanning direction is based on an analytical expression for an elliptical cylinder as follows [18, 19]:

$$f(x, y, z) \equiv \Theta[x - \psi(H - z)]\left(\frac{x - \psi(H - z)}{A}\right)^2 + \left(\frac{y}{B}\right)^2 + \left(\frac{z + C - H}{C}\right) - 1 = 0 \quad (7)$$
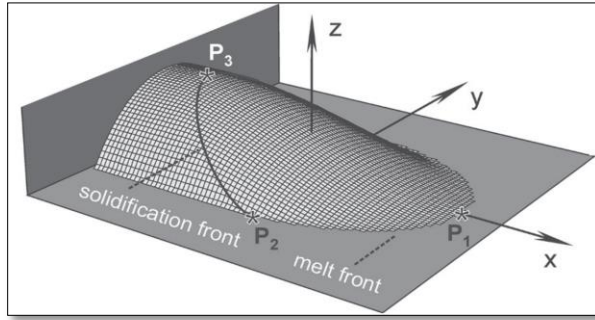

Fig. 4 Melting region and coating surface based on to the modified ellipsoid model [18].

FEM model

A 3-D thermal transient model based on the experimental geometry characteristics is developed by ANSYS 11.0. The SOLID-70 element with an 8-node linear brick shape was used in this model, and a non-uniform mesh was adopted for a higher density mesh in the irradiated area with a high thermal gradient. According to the mesh sensitivity study and a stable molten pool, the time increment (Δt) of 0.0015s was selected through a number of small time steps. The finest mesh size was 0.15 mm for the deposited area, and 1 mm was selected for the coarsest mesh size in the substrate far from the clad (Fig. 5).
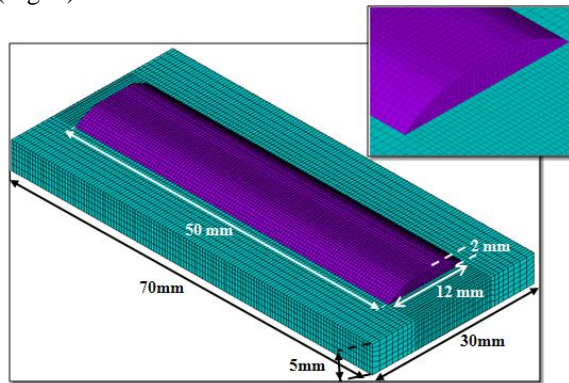

Fig. 5 The finite element meshed model.

Thermo-kinetic model and hardness prediction

In order to estimate the hardness distribution and solid-state phase transformation, the temperature evolution calculated from the thermal model was combined with the thermo-kinetic relations.

The phase transformation in a typical steel-based deposit by LC yields to changing the carbon solubility at different temperatures and thermal loading cycles. During the LC process, the temperature of the molten pool reaches 100% above the AC_3 (i.e., end temperature of austenite transformation). Therefore, the phase of solidified metal at the temperature upper than AC_3 is a fully homogenous austenite. According to the cooling rate in the LC process and based on the time-temperature-transformation (TTT) diagram shown in Fig. 6, the phase transformations during the cooling cycle can be estimated.
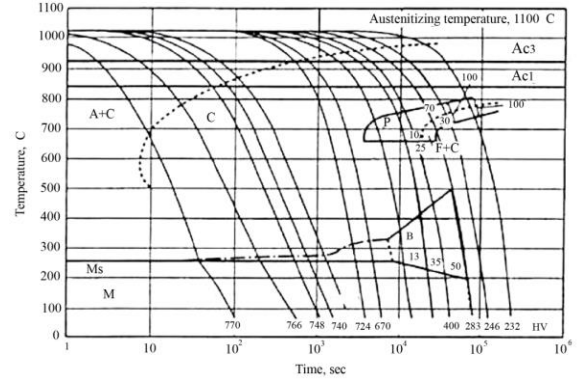

Fig. 6 TTT diagram of AISI H13, A: austenite, C: cementite, B: bainite, P:perlite, and M: martensite [33].

Considering the main phase transformation during the cooling process is a martensite transformation due to the sharp cooling rate (10^3-10^6 ^{o}C/s), there is not enough time for carbon diffusion to transform it into other possible phases [34]. The Koisten-Marburger equation was used to calculate the proportion of the martensite phase based on the cooling temperature. The volume fraction of the transformed martenise (f_m) is defined by Eq.8 [4, 35]:

$$f_m = 1 - f_y \cdot \varphi(T)$$

$$\varphi(T) = \begin{cases} 1, & \text{if } T \geq M_s \\ \exp(-0.011 \cdot (M_s - T)) & \text{if } T < M_s \end{cases} \quad (8)$$

where f_y is a volume fraction of austenite and φ is a function dependent on the cooling temperature and M_s. This equation applies to a wide range of ferrous metals [4]. The austenite volume fraction was calculated also according to the cooling temperature, AC_1 and AC_3 by using Eq.9 [34]:

$$f_y = \begin{cases} 0 & T < A_{C_1} \\ \dfrac{T - AC_1}{AC_3 - AC_1} & A_{C_1} < T < A_{C_3} \\ 1 & T > A_{C_3} \end{cases} \quad (9)$$

where f_y is a volume fraction of austenite and φ is a function dependent on the cooling temperature and M_s. This equation applies to a wide range of ferrous

metals [4]. The austenite volume fraction was calculated also according to the cooling temperature, AC_1 and AC_3 by using Eq.9 [34]:

$$M_s(^\circ C) = 539 - 423C - 30.4Mn - 12.1Cr - 7.5Mo - 7.5Si \tag{10}$$

At each temperature in the thermal loading cycle, the micro hardness of the deposited layer could be estimated fairly well based on the volume fractions of austenite (f_y) and martensite (f_m) and their corresponding hardnesses [4]:

$$H = f_y H_y + f_m H_M \tag{11}$$

where H_y and H_M are the hardness of austenite and martensite phase, respectively. According to the thermal history in LC, the hardness of martensite is estimated based on the model developed by Reti et al. [37]:

$$H_M = H_{M0} - A.\left[\int_0^t e^{-Q/R.T(t)}\right]^n \tag{12}$$

where H_{M0} is the regular hardness of the martensite, Q is the activation energy, R is the universal gas constant, A and m are the fitting constants, and T(t) is the time-dependent temperature that is obtained simultaneously from the thermal model. The values of the constants, activation energy, and phase transformation temperatures for AISIH13 are summarized in Table 4.

Table 4 The assumed values of the parameters used in thermo-kinetic modeling of AISI H13[38].

| Parameter	Description	Value
A_{c1}	Austenization start temperature ($^\circ$C)	919
A_{c3}	Austenization end temperature ($^\circ$C)	1069
H_y	Austenite hardness (HV)	250
M_s	Martensite transformation start temperature ($^\circ$C)	285
M_f	Martensite transformation end temperature ($^\circ$C)	100
H_{M0}	Martensite hardness (HV)	750
n	Empirical parameter	0.06
R	Universal gas constant (J/molK)	8.314
A	Empirical parameter (HV/sec)	1900
Q	Activation energy (KJ/mol)	244.37

Results and discussion

In this study, a 3-D transient heat transfer model was developed to estimate the temperature history of depositing H13 steel on mild steel A36 by HPDDL. The modeled temperature was coupled with thermo-kinetic empirical relations to predict the hardness distribution in the coating layer. In order to validate the computed results for temperature history and hardness distribution, a series of experiments were performed.
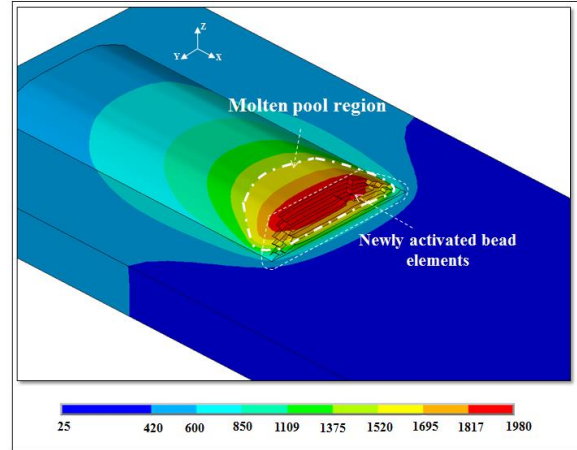
Fig. 7 Calculated temperature distribution in $^\circ$C, molten pool area, and 3-D view of activation element for generation the inclined molten surface.

Thermal model and its validation

The simulation result for temperature distribution in the process domain is shown in Figure 7. This figure presents the shape of the molten pool based on elliptical cylinder model for the activation element (Eq.7). The isotherm boundary at the melting temperature of a clad H13 (1480 $^\circ$C) is regarded as the molten pool edge, as shown in Fig. 7.presented by dashed lines. The minimum discrepancies between modeled and measured results were achieved when the thermal conductivity was enhanced by multiplying it with a factor of 2.6 along the x and y directions at temperatures higher than the melting point. The peak temperature at the position of TC_2 (550 $^\circ$C) is higher than TC_1 (500 $^\circ$C), and it could be attributed to laser energy accumulation that increased the substrate temperature gradually during LC.
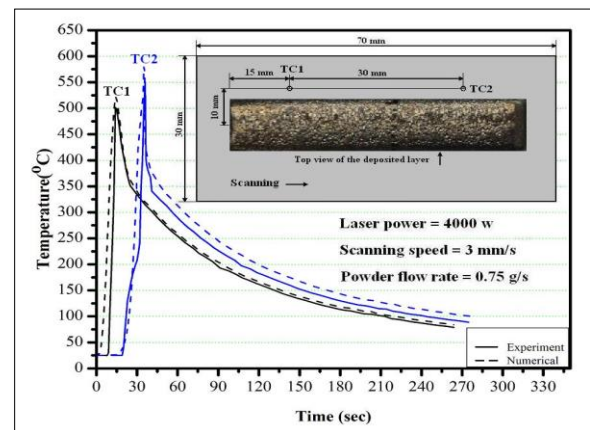

Fig. 8 Comparison between experimental and numerical temperature evolution

7

## Computed temperature gradient, heating and cooling rate

The temperature distribution across the clad is the basic data for the hardness estimation. Based on the temperature evolution at each position, the heating rate (ε_H), cooling rate (ε_C), thermal gradient (G), and corresponding hardness distribution (HV) were calculated. Figure 9 presents the isotherms across the clad-cross section. The maximum temperature (1940 ^{o}C) occurs at the top of the deposit that is 460 ^{o}C higher than the melting temperature of the clad material H13 (1480 ^{o}C). The temperature history across the cross-section is shown for the six different positions (see Fig 9.a), and the corresponding isotherms, representing the different thermal history in the cross-section of the cladded coupon are shown in Fig 9.b. The clad area is characterized with high thermal gradient isotherms that gradually became shallower by crossing the clad and substrate interface line because of the heat lost by conduction. In HAZ the temperature is below the melting temperature and above the AC_1 line (the starting temperature for austenite phase formation). This temperature gradience in this area means the phase transformations occurs in a solid state.
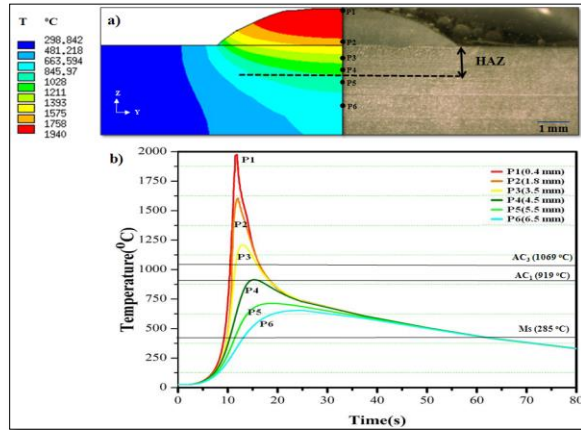
Fig. 9 (a) Numerical simulation of the heat transfer through the half of clad cross-section in comparison with a half of the cross-section of experimental coupon, (b) calculated temperature history with respect to time

Modeled temperature evolution across the cross section of the cladded coupon is used as the initial data to calculate the heating rate (ε_H), cooling rate (ε_C), and temperature gradient (G). The heating and cooling rates are a derivative of temperature with respect to time (dT/dt) in the heating and cooling cycles, respectively. The temperature gradient (G) along the thickness of the coupon is a derivative of temperature with respect to distance (dT/dz). Figure 9 represents the predicted value along the cross section. The experimental conditions are the same as shown

in Fig.8 for the temperature gradient and heating and cooling cycles.
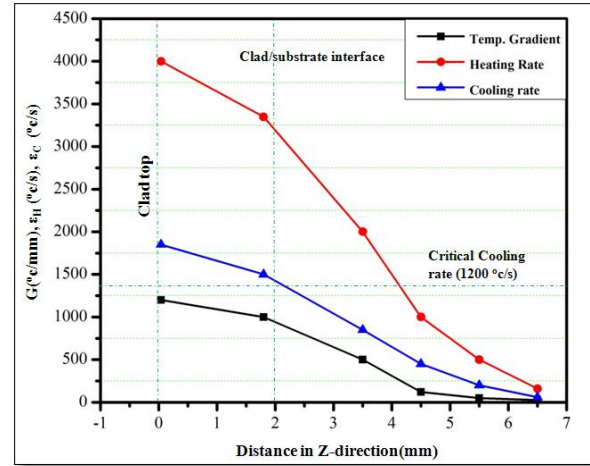
Fig. 10 Modeled temperature gradient (G), heating rate (ε_H), cooling rate (ε_C) across the thickness of cladded coupon from top of the clad to substrate

It could be observed from Figure 10 that the highest value for temperature gradient was at the top surface of the deposit (1200 ^{o}C/mm). This value gradually decreases to 850 ^{o}C/mm near the interface of the clad to the substrate. At the interface of clad and substrate, the temperature gradient sharply decreased (from 850 ^{o}C/mm to 500 ^{o}C/mm) and finally reached 60 ^{o}C/mm at the bottom of the substrate. This decrease means there was no influence of the temperature variation at the bottom of the substrate. The variations of heating and cooling rates in the clad area were from 4000 ^{o}C/s to 3250 ^{o}C/s and 1800 ^{o}C/s to 1400 ^{o}C/s, respectively. As it is shown in Figure 10, the calculated range of the cooling rate in the deposited layer was higher than the critical cooling rate (1200 ^{o}C/s) and a steeper cooling rate was produced at the top surface of the clad due to its maximum temperature [10].

Microstructure evolution

The microstructure evolution, grain size and consequently deposition hardness were affected by the variation in the cooling rate. Figure 11 represents the microstructure of the cross-section of the deposited layer with 4000 W of laser power, 3 mm/s of scanning speed, and 0.75 g/s of powder flow rate.
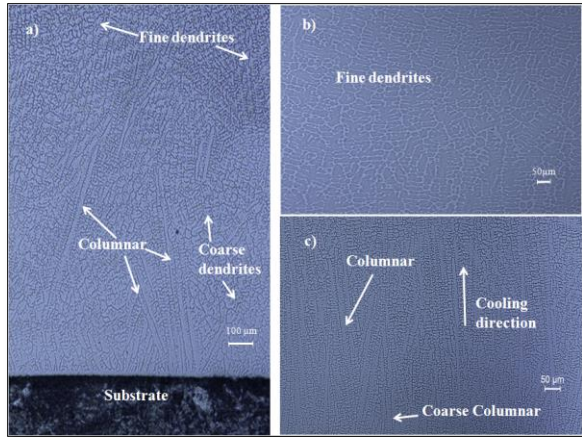
Fig. 11 Optical micrograph (1000X) of deposited layer a) Microstructure of clad, b) higher resolution of top of the clad, c) higher resolution of bottom of clad and near to the substrate interface

From Figure 11 the following can be concluded: the dendrites growth direction is mostly perpendicular to the substrate, opposite to the resultant heat flux, and parallel to the cooling direction [39]. The microstructure of the deposit layer consists of three regions. The bottom region is mostly a columnar structure with coarse dendrites (Fig 11.c) and the average size of the grain in this area is about 13 µm. The average grain size, at the middle of the deposited layer is over 10 µm and at the top of clad, a fine dendritic cellular exists (Fig 11.b) with an average grain size of 5 µm. The variation of grain size along the clad thickness is mainly attributed to the different levels of heating and cooling rates along the clad thickness (around 400 ^{o}C/s) [34]. As it is presented in Figure 10, the top of the clad area has very high heating and cooling rates that induce a very fine dendrite microstructure. Upon approaching the interface, the microstructure is a mixture of coarse dendrites and a first-arm columnar structure. Finally at the interface of the deposited layer and substrate, the microstructure is formed by coarse columnar that is perpendicular to the scanning direction and oriented along the cooling direction.

**Hardness prediction based on thermo-kinetic model**

In LC, the thermal properties of the coating material govern the microstructure of the deposit and subsequently decide the hardness distribution. In this study, the temperature evolution calculated by the thermal model was combined with thermo-kinetic relations to estimate the hardness distribution. Figure 12 presents the temperature, austenite fraction, and hardness vs. time for the position denoted by a point

1 in Fig. 9. At this position, the temperature in the time domain of (10.5-16.8 s) was higher than AC_1, and the austenite fraction in this time domain increased gradually (from 0 to 1). In the cooling phase after crossing the AC_1 temperature, the austenite fraction reached zero and fully transformed to martensite after reaching the M_f temperature. Figure 12.c represents the hardness changes during the heating and cooling cycles. By the formation of the austenite phase, the initial hardness starts from 250 HV (initial hardness of austenite). On the other hand, in the cooling process with the phase transformation of austenite to martensite, the hardness increased until reaching the final value of 707 HV below the M_f temperature. The hardness of martensite for each individual temperature was calculated based on Eq. 12, and the final hardness of the deposit was calculated according to the austenite and martensite volume fractions and their corresponding hardness.
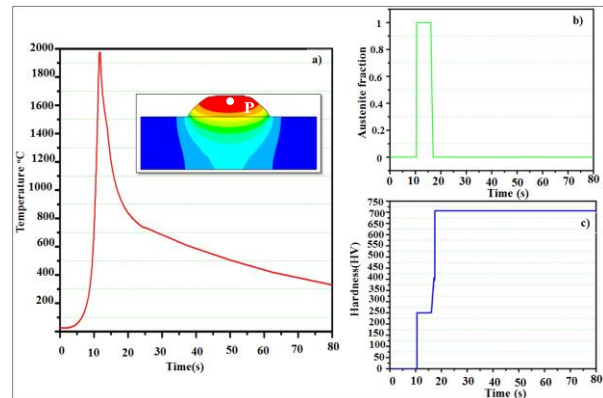
Fig. 12 (a) Distribution of temperature (a), austenite fraction (b), and hardness *vs* time (c) for pint 1 with laser power of 4000 kW, scanning speed of 3 mm/s, and powder flow rate of 0.75 g/s.
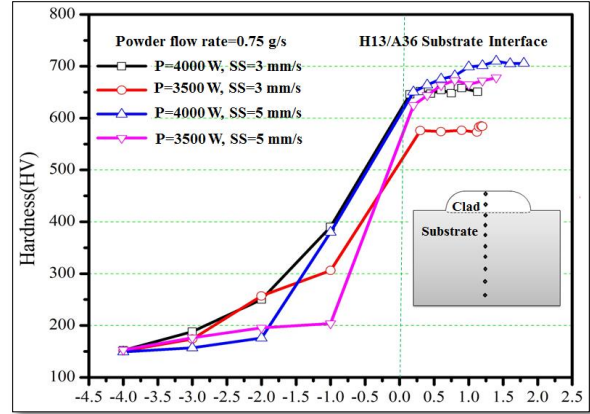
The same calculation was performed for different positions along the clad thickness to estimate the corresponding hardness distribution across the deposited layer. In order to validate the modeled hardness, the calculated values were compared with the measured ones. Figure 13 represents the comparison between modeled and measured hardness for two different experimental conditions. A good agreement between the numerical and experimental results can be found.

9
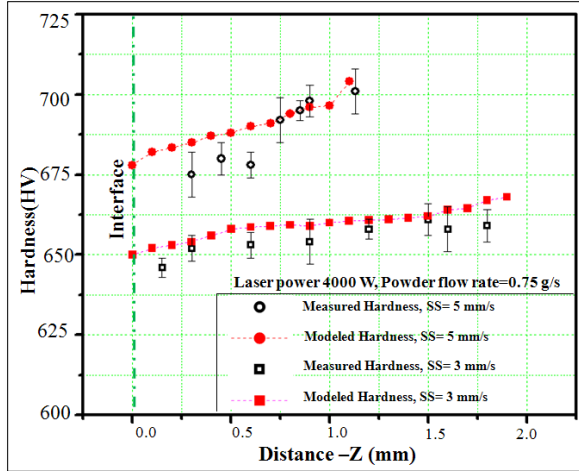
Fig. 13 Measured and predicted hardness along the thickness of clad for experimental conditions: laser power 4000 w, powder flow rate 0.75 g/s, and scanning speed 5 mm/s and 3 mm/s.

Fig. 14 Hardness measurements of four experimental conditions.

Under the experimental conditions for case (a), the measured and modeled hardness gradually increased from the interface to the top of the deposit, from 675 HV to 701 HV and from 678 HV to 708 HV, respectively. In the same manner for the experimental conditions for case (b) the variations of modeled and measured hardness were 576 HV to 584 HV and 568 HV to 591 HV, respectively. The main reason for this distribution was related to the corresponding microstructures and the hardness that remained in the clad. The coarse microstructure and corresponding lower hardness at the region near to the interface was mainly attributed to the relatively lower peak temperature and slower cooling rate. In this study, the level of dilution was in micro-scale, which is clear in the micrograph of the cross section of the cladded coupon in Figure. 3. In addition, a chemical composition of the deposited layer was uniform through the cross section of the clad according to the EDS spectrum data. Therefore, dilution with substrate does not have any remarkable effect on hardness reduction above the interface. The discrepancy between modeled and measured hardness could be attributed to the error in fitting the constants in the thermo-kinetic model that were adapted from Ref. [38] for H13.

The influence of the laser power and scanning speed on the microhardness distribution of the deposited layer was taken into account as shown in Figure 14. The microhardness along the coupon thickness from the bottom to the top was measured by a digital micro-hardness tester.

Figure 14 indicates that at the same scanning speed and powder flow rate, the higher laser power leads to a higher hardness in the clad because of a relatively higher peak temperature and steeper cooling rate. According to the measured data, the microhardness changed from 678 HV to 584 HV by decreasing the scanning speed from 5 mm/s to 3 mm/s under the same laser power of 3500 W; and from 678 HV to 706 HV when laser power was increased from 3500 W to 4000 W with the same scanning speed of 5 mm/s. Therefore, it could be concluded that the final hardness is more sensitive to change in the scanning speed than change in laser power.

Conclusions

In LC, the final hardness distribution of the clad usually depends on temperature history. In this study, an experimentally validated 3-D heat transfer model was developed to further study the temperature evolution and heating and cooling rates during the deposition of H13 by HPDDL. The results from the thermal model are coupled with the thermo-kinetic relations in order to estimate the deposit hardness. Based on the presented results, the major conclusions are as follows:

1. The cooling rate gradually decreases from top to bottom of the clad as a result of the reduction in temperature gradient going from the top to the bottom of the clad.
2. The changes of the cooling rate along the deposit, affects the final hardness distribution where a steeper cooling rate induces a higher value of hardness.
3. The microstructure study showed that the existing microstructure contains finer dendrites near the top surface of the deposit that has a

relatively higher temperature and steeper cooling rate.
4. The calculated thermal cycles and hardness distribution of H13 deposition were in good agreement with the experimental measurements.
5. The final hardness was more affected by the change in the scanning speed than in the laser power. By increasing the scanning speed form 3 mm/s to 5 mm/s, the average measured hardness changed from 584 HV to 678 HV.
6. The developed model could be used for the thermal field estimation in H13 deposition by HPDDL as well as optimization of the process parameters in order to achieve the desired hardness distribution.

Acknowledgment

References

[1]. **Mazumder, J. A. Schifferer, and J. Choi**., 1999. "Direct materials deposition: designed macro and microstructure." Materials Research Innovations 3. pp.118-131.

[2]. **Sears, James W**., 1999. "Direct laser powder deposition-'State of the Art". No. KAPL-P-000311; K99089. Knolls Atomic Power Lab., Niskayuna, NY (US).

[3]. **Toyserkani, Ehsan, and Amir Khajepour**., 2006, "A mechatronics approach to laser powder deposition process", Mechatronics 16.10. 631-641.

[4]. **Costa, L., Vilar, R., Reti, T., & Deus, A. M.**, 2005. "Rapid tooling by laser powder deposition: Process simulation using finite element analysis". Acta Materialia, 53(14), pp.3987-3999.

[5]. **Foroozmehr, Ehsan, and Radovan Kovacevic**., 2010, "Effect of path planning on the laser powder deposition process: thermal and structural evaluation". The International Journal of Advanced Manufacturing Technology 51.5. pp.659-669.

[6]. **He, X., G. Yu, and J. Mazumder**., 2009, "Temperature and composition profile during double-track laser cladding of H13 tool steel". Journal of Physics D: Applied Physics 43.1 015502.

[7]. **Picasso, M., Marsden, C. F., Wagniere, J. D., Frenk, A., & Rappaz, M**., 1994. "A simple but realistic model for laser cladding". *Metallurgical and Materials Transactions B*, *25*(2),pp.281-291.

[8]. **Hofman, J. T., De Lange, D. F., Pathiraj, B., &Meijer**, J., 2011. "FEM modeling and experimental verification for dilution control in laser cladding". Journal of Materials Processing Technology, 211(2), pp.187-196.

[9]. **J.Mazumder and W.M.Steen., 1980,** J.Appl.Phys, 51,941.

[10]. **Kar, A., and J. Mazumder**., 1987, "One-dimensional diffusion model for extended solid solution in laser cladding". *Journal of applied physics* 61.7. pp.2645-2655.

[11]. **Kim, Jae-Do, and Yun Peng**., 2000, "Plunging method for Nd: YAG laser cladding with wire feeding". Optics and lasers in engineering 33.4. pp.299-309.

[12]. **Amara, E. H., L. Achab, and O. Boumia**., 2005, "Numerical modelling of the laser cladding process using a dynamic mesh approach". Advanced Optoelectronics and Lasers. Proceedings of CAOL 2005. Second International Conference on. Vol. 1. IEEE.

[13]. **Kong, Fanrong, and Radovan Kovacevic**., 2010, "Modeling of heat transfer and fluid flow in the laser multilayered cladding process". Metallurgical and Materials Transactions B 41.6 pp.1310-1320.

[14]. **Wen, Shaoyi, and Yung C. Shin**., 2011, "Modeling of the off-axis high power diode laser cladding process". Journal of heat transfer 133.3.

[15]. **Toyserkani, Ehsan, Amir Khajepour, and Steve Corbin**., 2004, "3-D finite element modeling of laser cladding by powder injection: effects of laser pulse shaping on the process." Optics and Lasers in Engineering 41.6. pp.849-867.

[16]. **Fallah, V., Alimardani, M., Corbin, S. F., & Khajepour, A.,** 2011. "Temporal development of melt-pool morphology and clad geometry in laser powder deposition". Computational Materials Science, 50(7), pp.2124-2134.

[17]. **Kumar, S., Roy, S., Paul, C. P., & Nath, A. K**., 2008 . "Three-dimensional conduction heat transfer model for laser cladding process". Numerical Heat Transfer, Part B: Fundamentals, 53(3), pp.271-287.

[18]. **Brückner, F., D. Lepski, and E. Beyer**., 2007, "Modeling the influence of process parameters and additional heat sources on residual stresses in laser cladding."*Journal of thermal spray technology* 16.3. pp.355-373.

[19]. **Balu, Prabu, Syed Hamid, and Radovan Kovacevic**. "Finite element modeling of heat transfer in single and multilayered deposits of Ni-WC produced by the laser-based powder deposition process." The International Journal of Advanced Manufacturing *Technology* (2013): 1-14.

[20]. **Li, M. V., Niebuhr, D. V., Meekisho, L. L., & Atteridge, D. G**., 1998 . "A computational model for the prediction of steel hardenability". *Metallurgical and Materials transactions B*, *29*(3), pp.661-672.

[21]. **Wang, Liang, and Sergio Felicelli**., 2007, "Process modeling in laser deposition of multilayer SS410 steel." transactions-american society of mechanical engineers journal of manufacturing science and engineering 129.6 1028.

[22]. **Manvatkar, V. D., Gokhale, A. A., Jagan Reddy, G., Venkataramana, A., & De, A**., 2011. "Estimation of Melt Pool Dimensions, Thermal Cycle, and Hardness Distribution in the Laser-Engineered Net Shaping Process of Austenitic Stainless Steel". Metallurgical and Materials Transactions A, 42(13), pp.4080-4087.

[23]. **Li, Lin**., 2000, "The advances and characteristics of high-power diode laser materials processing". Optics and Lasers in Engineering 34.4.pp.231-253.

[24]. **Lisiecki, A., and A. Klimpel**., 2008, "Diode laser surface modification of Ti6Al4V alloy to improve erosion wear resistance". Archives of Materials Science and Engineering 32.1. pp.5-12.

[25]. **Cook, C. M., Haake, J. M., Zediker, M. S., & Banaskavich, J. M.**, 2000,. "Diode laser cladding produces high quality coatings". In International SAMPE Technical Conference (32) 910-921.

[26]. **Taktak, Sukru**., 2007, "Some mechanical properties of borided AISI H13 and 304 steels". Materials & design 28.6 .1836-1843.

[27]. **Mazumder, J., Choi, J., Nagarathnam, K., Koch, J., & Hetzner, D**., 1997. "The direct metal deposition of H13 tool steel for 3-D components". JOM Journal of the Minerals, Metals and Materials Society, *49*(5), 55-60.

[28]. Handbook, Metals. "vol. 2." ASM, Materials Par, OH (1990).

[29]. **Nadimi, S., Khoushehmehr, R.J., Rohani, B., Mostafapour, A**., 2008. "Investigation and analysis of weld induced residual stresses in two dissimilar pipes by finite element modeling". Journal of Applied Science 8, 1014–1020.

[30]. **Capello, E., Castelnuovo, M., Previtali, B., & Vedani, M**., 2007. "Surface treatment of welded duplex stainless steels by diode laser". Journal of Laser Applications, 19(3), 133-140.

[31]. **NASH, P., Hu, Z., Zhou, G., & Adak, B.,** 2004. "Molten Pool Size in Laser Cladding Simulated by Finite Element Method". Materials Science & Technology (MS&T'04), 303-311.

[32]. **Yafei, S., Yongjun, T., Jing, S., & Dongjie, N**., 2009. "Effect of temperature and composition on thermal properties of carbon steel". In Control and Decision Conference, 2009. CCDC'09. Chinese 3756-3760.

[33]. **Prabhudev, K. H.** Handbook of heat treatment of steels. Tata McGraw-Hill Education, 1988.

[34]. **Gür, Cemil Hakan, and Jiansheng Pan**. Handbook of thermal process modeling of steels. CRC PressI Llc, 2009.

[35]. **KOISTINEN.P**,**MARBURGER**,Acta Metall., 1959, 7, 59.

[36]. **KW Andrews**. J Iron Steel Inst 1965; 203:721.

[37]. **Reti, T., Gergely, M., Tardy, P.,** 1987, "Mathematical treatment of non-isothermal transformation". Materials Science and Technology 3(5), 365-371

[38]. **Golozar, M. A.,** 2001, Principles and Applications of Heat Treatment of Steels. .

[39]. **Dinda, G. P., A. K. Dasgupta, and J. Mazumder**., 2009, "Laser aided direct metal deposition of Inconel 625 superalloy: Microstructural evolution and thermal stability". Materials Science and Engineering: *A* 509.1. 98-104.